Science Advances
AAAS

advances.sciencemag.org/cgi/content/full/5/8/eaav3971/DC1

Supplementary Materials for

Hypervelocity impacts as a source of deceiving surface signatures on iron-rich asteroids

Guy Libourel*, Akiko M. Nakamura, Pierre Beck, Sandra Potin, Clément Ganino, Suzanne Jacomet, Ryo Ogawa, Sunao Hasegawa, Patrick Michel

*Corresponding author. Email: libou@oca.eu

Published 28 August 2019, *Sci. Adv.* **5**, eaav3971 (2019)
DOI: 10.1126/sciadv.aav3971

This PDF file includes:

Section S1. Experimental and effect of surface roughness on the reflectance spectra of metallic meteorites

Experimental: Impact experiments were performed using a 7-mm bore two-stage light-gas gun at the Institute of Space and Astronautical Science (ISAS) in Japan. Projectile and ejecta trajectories are captured with a high-speed video camera (frame rate of 2 or 4 μs) that monitors the experiment.

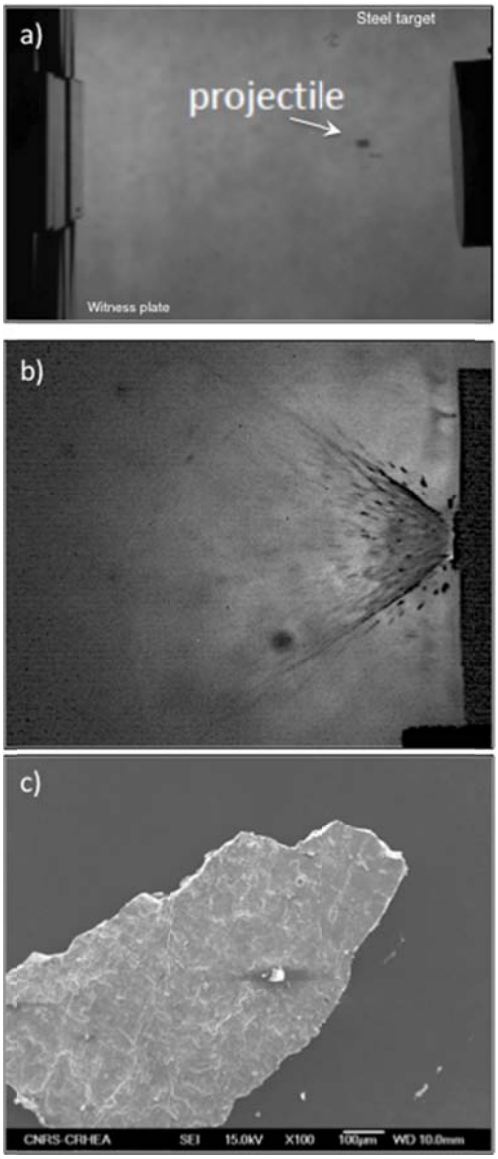

Fig. S1. Impact experiments. a) Projectile is a mm-sized basalt-like bead. Distance between the target and the aluminum witness plate is around 100 mm. The steel target has a diameter of around 60 mm in diameter. **b**) High-speed video camera (frame rate of 4 µs) monitors the impact and the trajectory of the ejecta. In this representative example, one can clearly observe the occurrence of large mm-sized shapeless fragments at the edge of the ejecta swarm, excavated from the metallic target (27). **c**) Secondary electron SEM image of one of the steel fragment recovered on the floor of the impact chamber (n0). Notice the well oriented deformation bands.

The spheroidal projectiles used for the steel targets consisted of millimeter-sized glass beads. Dunite and basalt projectiles were cut from pristine leftover targets of previous impact experiments (58, 59). Run conditions are summarized in table S1.

Table S1. Experimental conditions.

	Projectile	Note	Target	Impact velocity	Mass of the projectile	Energy
exp. number				km/s	g	J
n3	Basalt		Steel	3.39	0.033	190
n1	Basalt		Steel	4.9	0.037	444
n4	Basalt		Steel	6.88	0.03	710
n0	Basalt		Steel	6.89	0.08	1899
n5	Dunite		Steel	4.91	0.074	892
ND1	Basalt	dry	Steel	5.44	0.0448	710
NW2	Basalt	wet	Steel	5.41	0.0367	537
n101	Dunite		Gibeon	3.25	0.0454	240
n102*	Dunite	151 K	Gibeon	3.28	0.0458	246
n103	Dunite		Gibeon	6.97	0.0444	1078
n107*	Basalt	131 K	Gibeon	5.08	0.0381	492

Effect of surface roughness on the reflectance spectra of metallic meteorites:

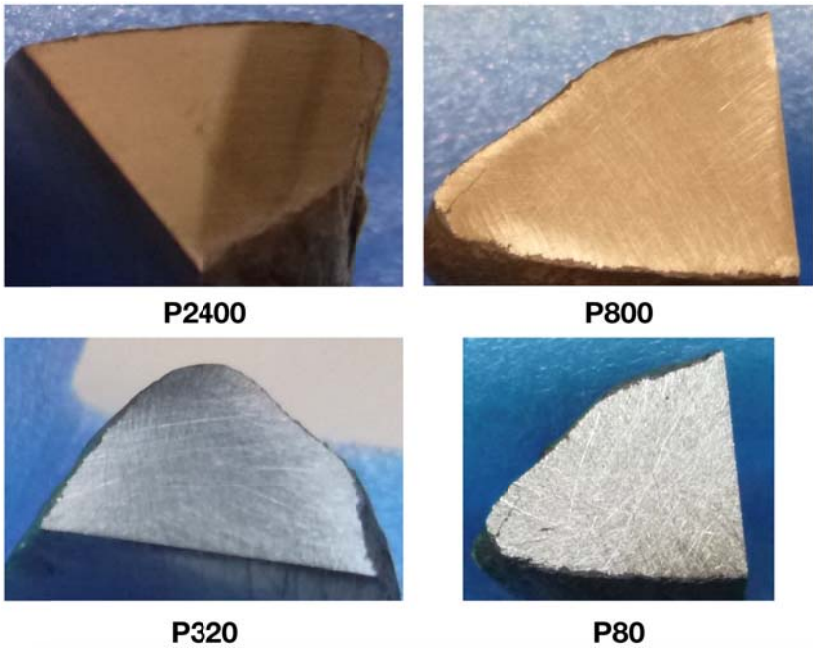

Fig. S2. Various surface roughness of the Gibeon iron meteorite. Pictures of the flat surface of the sample of the Gibeon meteorite after the four alterations by the abrasive disks P2400, P800, P320 and P80. Photo Credit: Sandra Potin, IPAG.

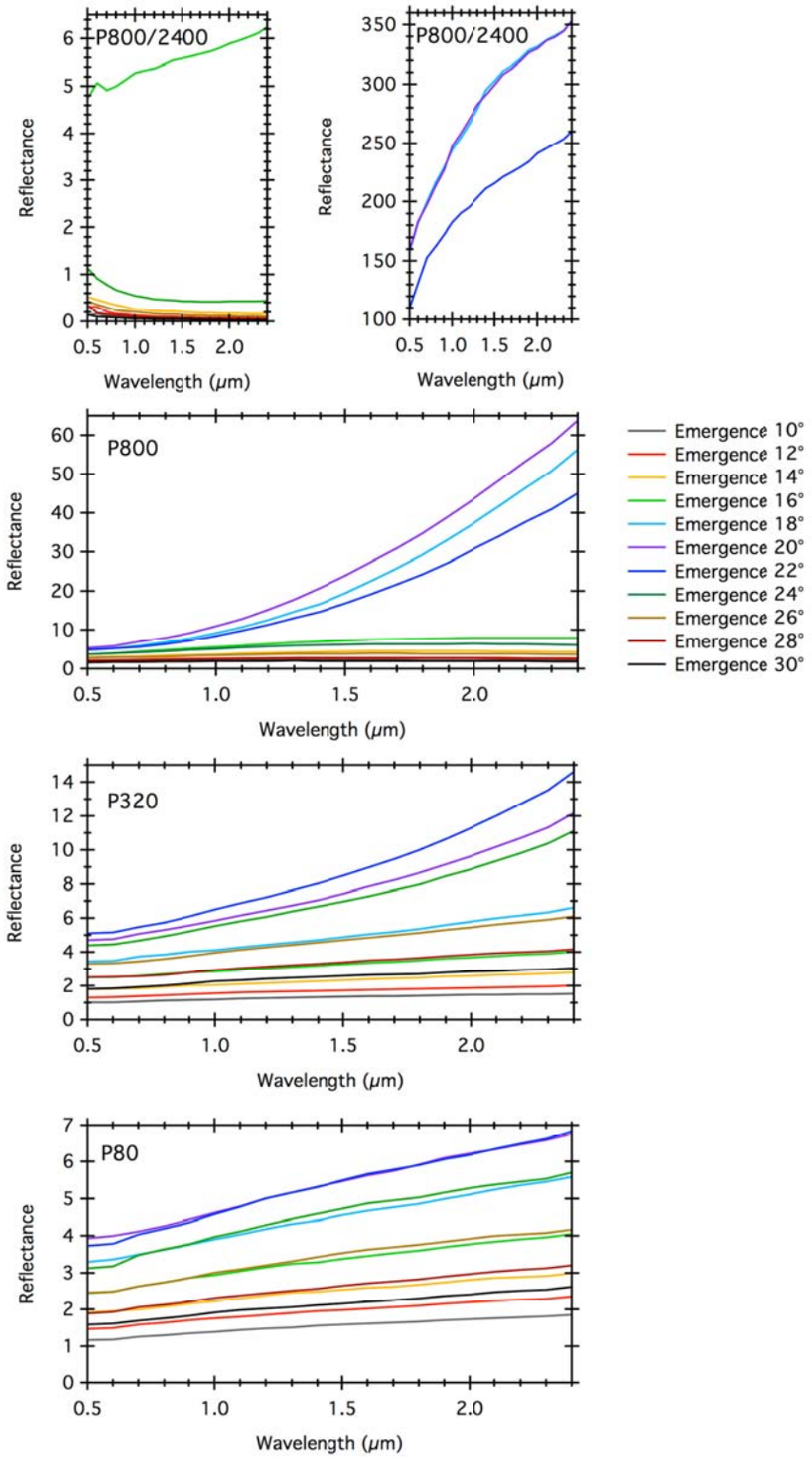
P800/2400
Reflectance
Wavelength (μm)
P800/2400
Reflectance
Wavelength (μm)
P800
Reflectance
Wavelength (μm)
Emergence 10°
Emergence 12°
Emergence 14°
Emergence 16°
Emergence 18°
Emergence 20°
Emergence 22°
Emergence 24°
Emergence 26°
Emergence 28°
Emergence 30°
P320
Reflectance
Wavelength (μm)
P80
Reflectance
Wavelength (μm)

Fig. S3. VIS-NIR spectra of the Gibeon meteorite after progressive roughening of the sample. From top to bottom the roughness of the surface was progressively increased by manually scratching with SiC disks. Spectra were measured with an incidence at 20° and under different emergence angle, within the principal plane (the specular direction is therefore around emergence=20°). The spectra reveal a strong dependence on observation geometry. In the case of the most finely polished surface (P800/2400), with a mirror like appearance, the reflectance is high in the specular direction (>100) and the spectra reveal a strong red slope. For spectra measured outside of the specular direction, the spectra are blue and the reflectance decreases when moving away from the specular direction. Spectra show a strong variability due to the surface roughness of the meteorite and the geometry of the system, incidence, emergence and azimut angles. Value of reflectance, as well as the spectral slope is impacted.

Section S2. Hypervelocity impact experiments on steel targets (more images and observations)

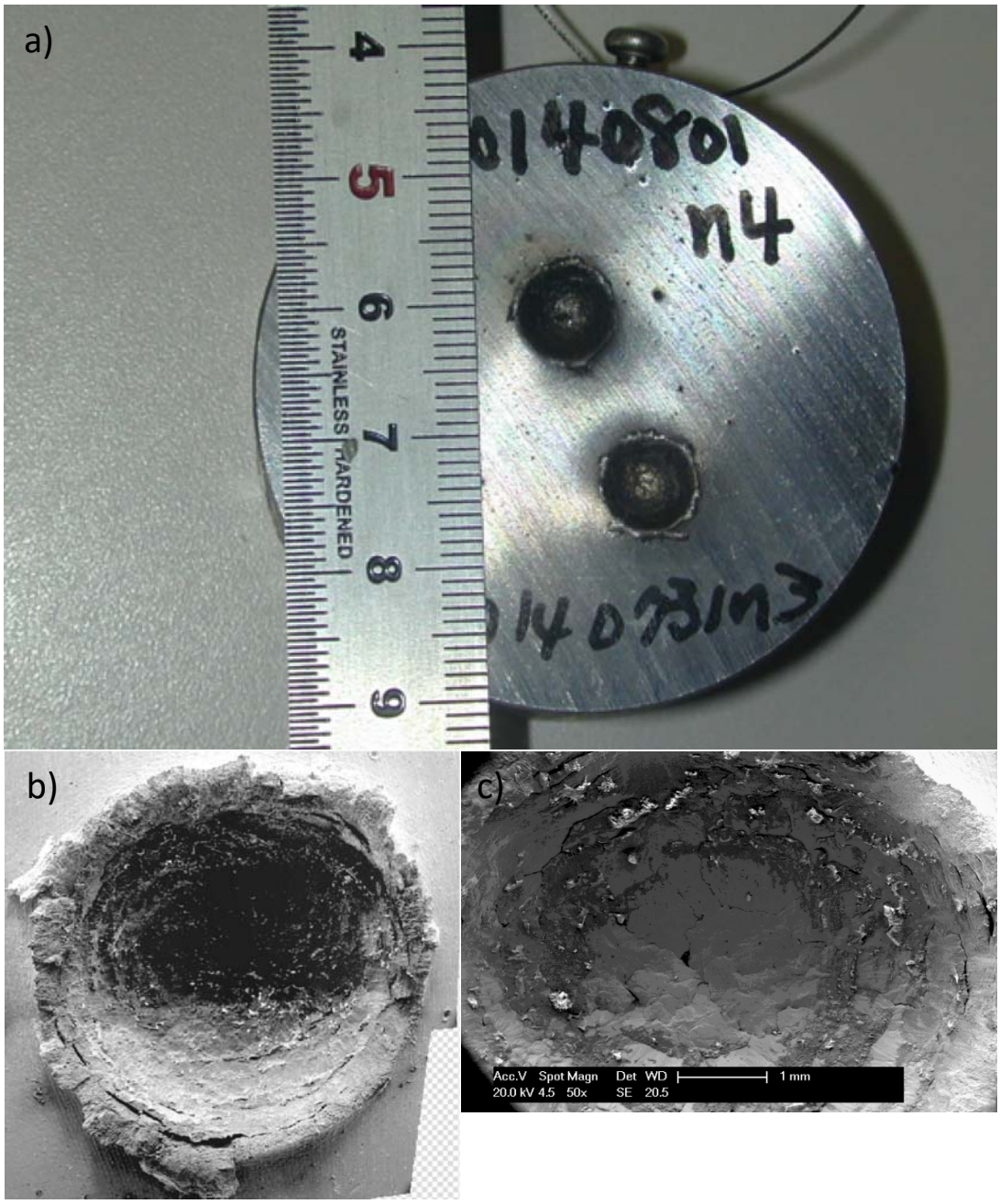

Fig. S4. Morphology of hypervelocity impact craters on steel target. a) Picture of n3 (3.39 km/s, 190 J) and n4 (6.88 km/s, 710 J) crater produced by hypervelocity impact of basalt-like millimeter sized beads on SCM 435 steel cylinder target. Note the darkening of the inside of the crater due to the coating of the basaltic impact melt (27). Photo Credit: Akiko M. Nakamura, Kobe University. **b**) and **c**) Secondary electron images of the n4 and n3 crater respectively coated with different amount of impact melt/glassy coating. Photo Credit: Suzanne Jacomet, Mines ParisTech)

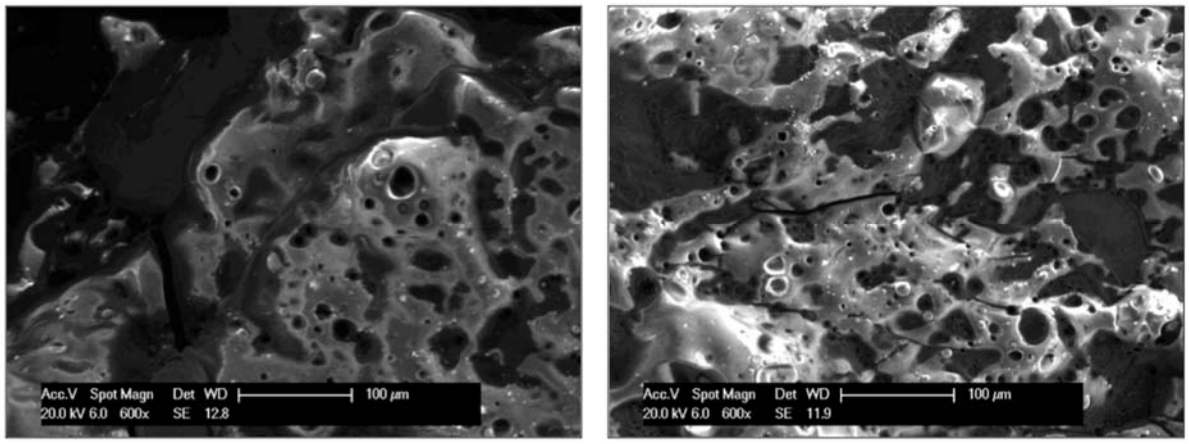

Fig. S5. Crater glassy coating characterization. Secondary electron microscopy (SEM) images of the inside edge of the n0 crater showing the basalt glassy coating with degasing features (left). Note the efficiency of the impact melt to almost completely coat the surface of metallic target. The glass coating is very often fractured due to the glass relaxation occurring at temperature below the glass transition temperature after the quench (right).

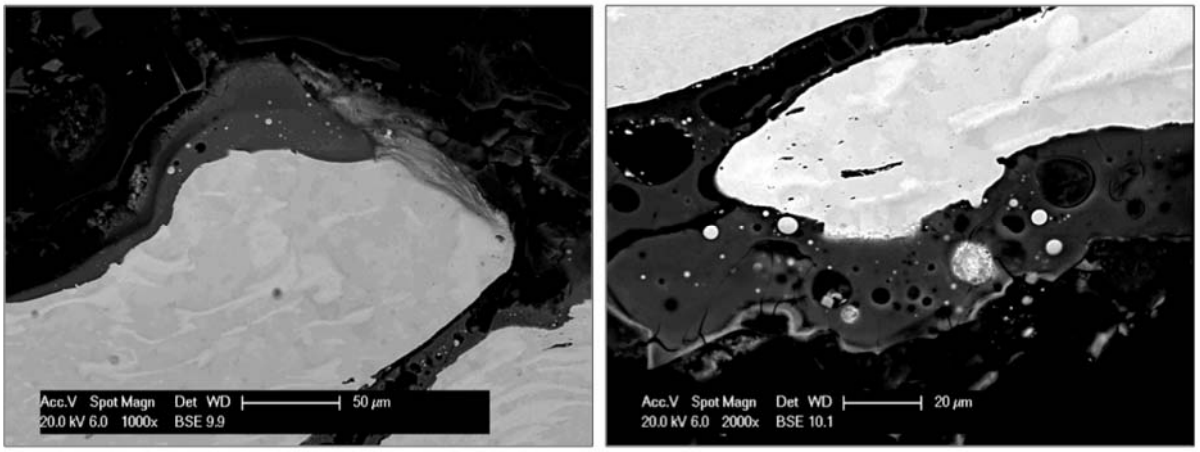

Fig. S6. Cross section of the impact melt glassy coating at the bottom of hypervelocity crater. Secondary electron microscopy (SEM) images of the inside edge of the n0 crater (details of the crater cross-section from Fig. 1D) showing the coating of the impact melt with degasing features. Notice the melt injection in fractures as well as the minute metal blebs due to reduction during the impact.

Section S3. Characteristics of impact melt coating inside hypervelocity craters

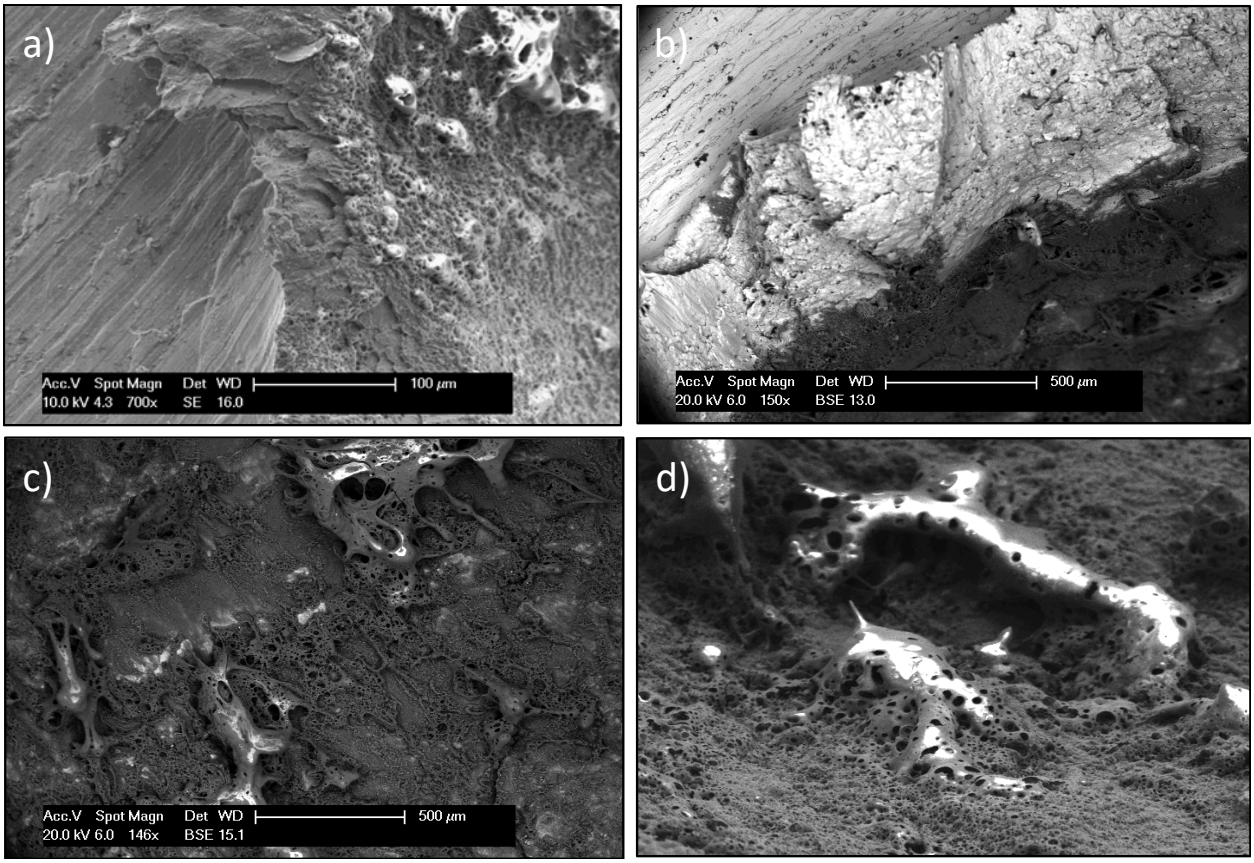

Fig. S7. Secondary electron microscopy (SEM) images of the impact melt coating inside craters caused by basalt-like projectiles. a) Secondary electron view of the external edge of the crater n1. Note spall fracture plane in the steel and the basaltic coating in the inside of the lip of the crater. **b**) Backscattered secondary image of the internal edge of the crater n1, showing how the basaltic impact melt (dark) coats efficiently the steel surface (light grey). **c**) Coating on the wall of the crater n1. Notice the structure in channels and teardrops of the coating, as well as the high vesicularity of its glassy surface. **d**) Example of smooth and foamy glass coating at the bottom of the crater #NW2.

Section S4. Hypervelocity impact of a dunite projectile on metallic target

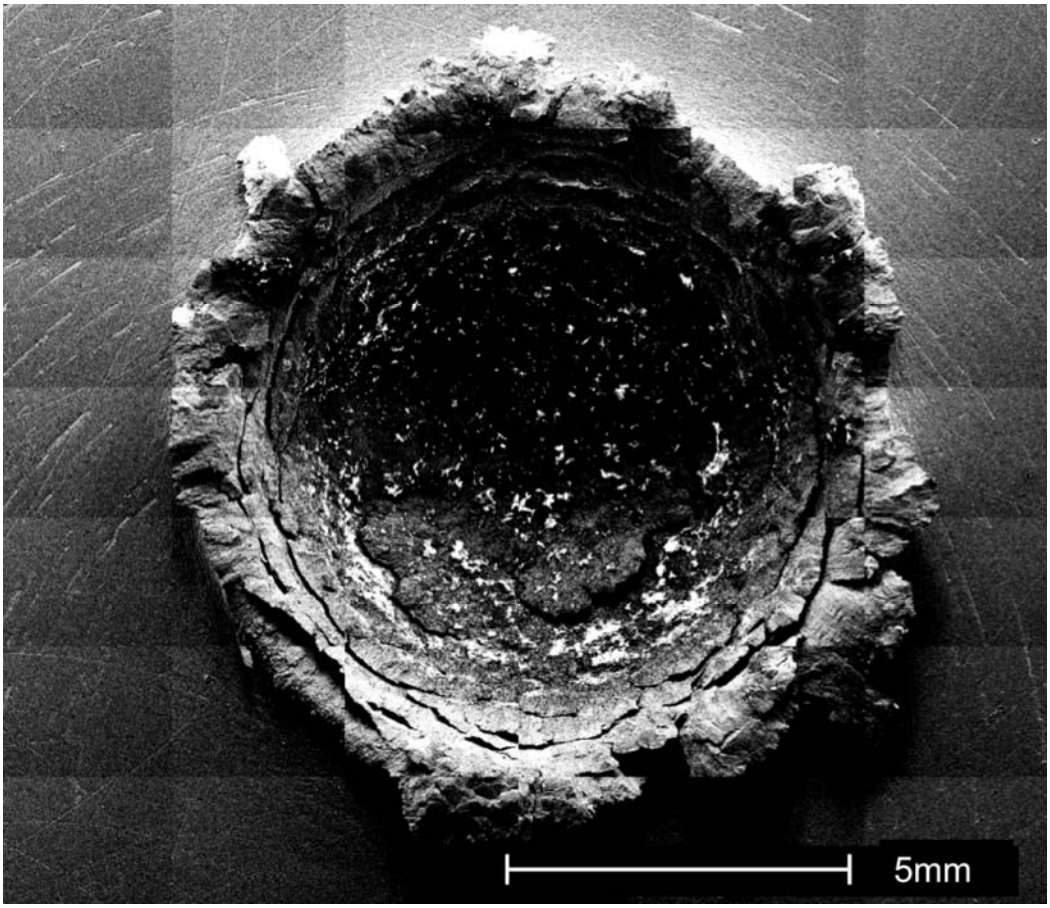

Fig. S8. Secondary electron microscopy (SEM) image of impact crater caused by a dunite projectile on steel target (n5; 4.91 km/s; 892 J). Notice the regular bowl-shape of the crater as well as the continuous metallic flap at its edge (27). The bottom of the crater is coated by the impact melt produced by the melting of the dunite during the impact. A clear network of concentric fractures is also observable. Comparison of this figure with the Fig. 1D allows interesting evaluations of how deep such networks of fractures penetrate the bottom of the metallic target.

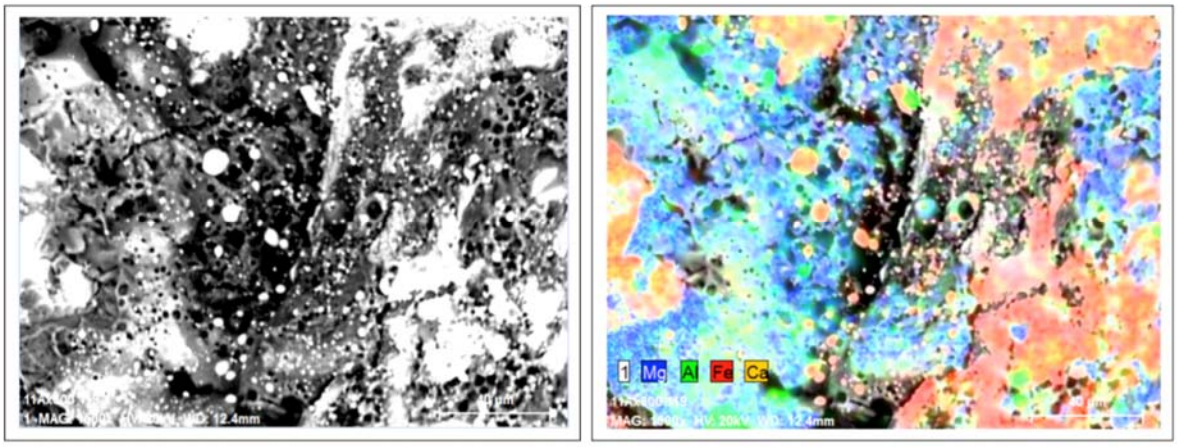

Fig. S9. Characterization of the crater coating of the molten dunite. (Left). Secondary electron microscopy (SEM) images of the inside edge of the metallic crater produced by dunite impact, and showing the coating of the molten dunite. The glassy dunite is peppered by small metal blebs associated with bubbles of degassing. (Right) Composite X-ray element map (Al: green; Mg: blue; Fe: red) of the same area of the n5 dunite crater (4.91 km/s; 892 J). The molten-dunite coating spreads efficiently over the entire surface of the bowl shape crater, in a similar way as molten basalt does. This allows to conclude that the same crater signature, including shape, coating, metal blebs and degasing, is produced whatever the nature of the projectile, crystallized (dunite) or glassy (basalt). Chondrite and achondrite materials should behave similarly, since dunite is overwhelmingly more refractory. Assuming a shock pressure of a few tens of GPa, the associated temperature should be in excess of 2000-2500 K according to melting temperature of dunite-like material at high pressure.

Section S5. Hypervelocity impact experiments on (Gibeon) iron meteorite target

a)
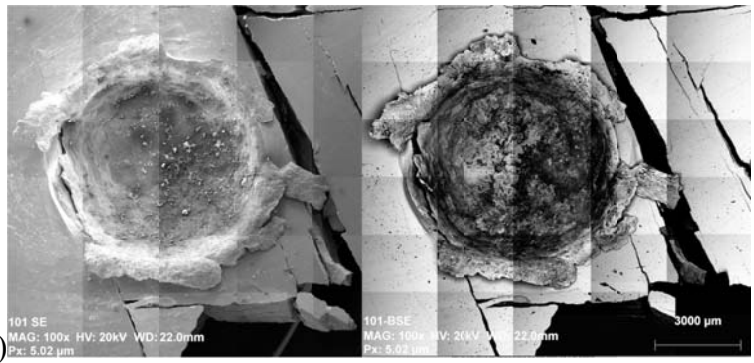

b)
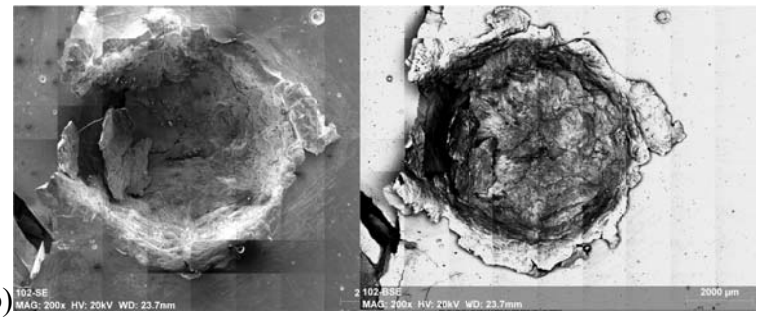

c)
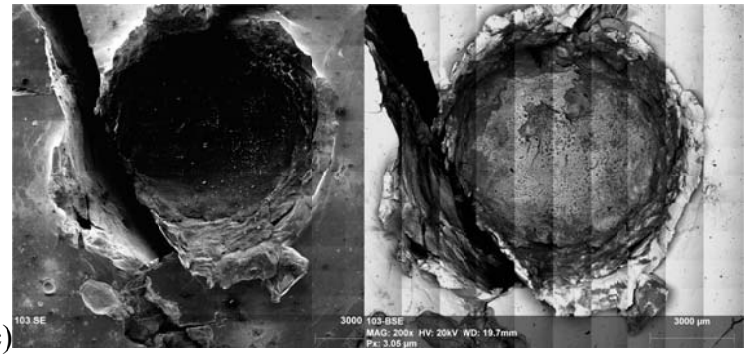

d)
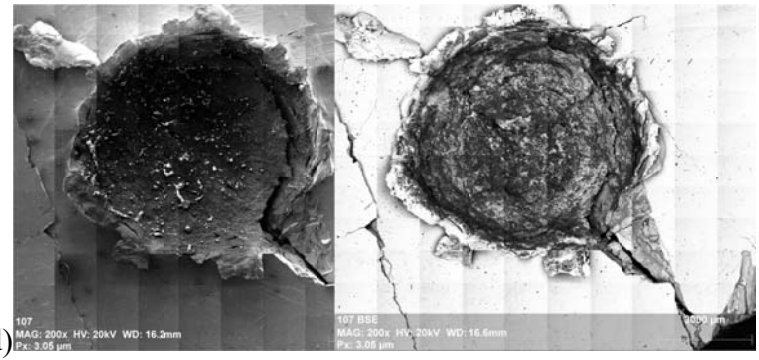

Fig. S10. Morphology of hypervelocity impact craters on Gibeon iron meteorite target. SE and BSE crater views: **a**) #101 dunite @ 3.25 km/s at room temperature, **b**) #102 dunite @ 3.28 km/s at 151 K, **c**) 103 dunite @ 6.97 km/s at room temperature, and **d**) 107 basalt @ 5.08 km/s at 131 K.

Section S6. Hypervelocity impact experiments using dry and hydrated basalt projectile on steel target

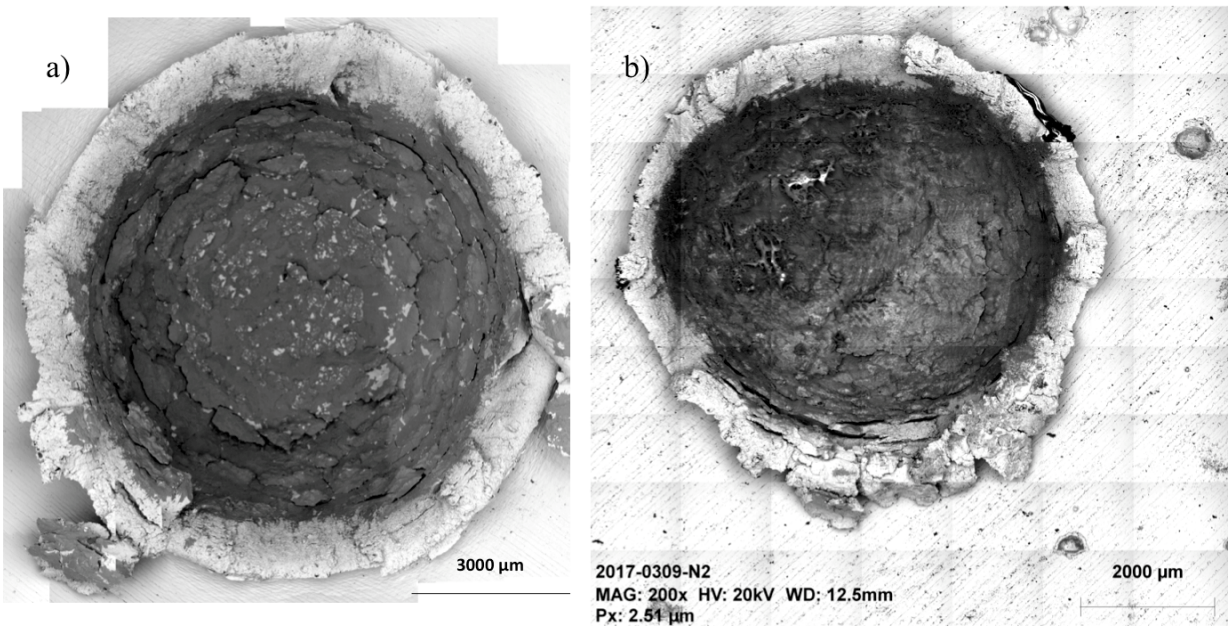

Fig. S11. Morphology of hypervelocity impact craters using dry and hydrated basalt projectile on steel target. BSE crater views of **a**) hypervelocity impact experiment ND1 (table S1) using a dry PST9 basalt projectile (Pichavant et al., 2009), and **b**) hypervelocity impact experiment NW2 (table S1) using a wet (3.3 wt% H_2O) PST9 basalt projectile (Pichavant et al., 2009). In this shot the projectile was partly broken due to acceleration before hitting the target. Corresponding VIS-NIR spectra are shown in Fig. 6.

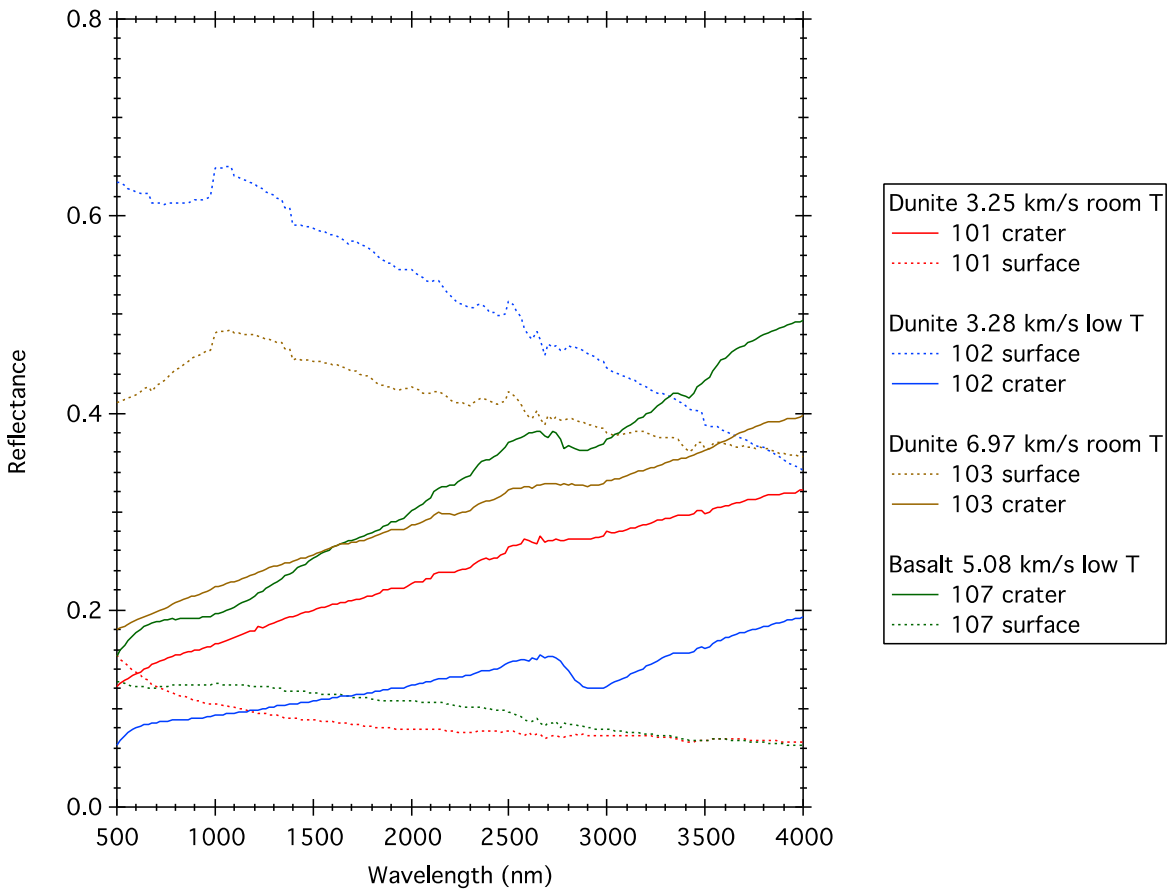

Fig. S12. VIS-NIR spectra of impact crater on Gibeon iron meteorite targets using dry dunite and basalt projectiles. Notice the strong absorption bands near 3 µm for experiments #102 and #107 performed at low temperature by comparison of those performed at room temperature despite the use of dry projectiles. Here, entrapment of water within impact glasses is due to the trap of the residual water moisture of the experimental chamber condensed at the Gibeon iron meteorite surfaces prior to the shots. This unexpected occurrence of a 3µm absorption bands shows however how sensitive NIR spectra could be to detect low hydroxyl concentrations in a glassy matrix.